Mem. S.A.It. Vol. 87, 425

Memorie della

Cosmological models of galaxy formation

N. Menci

Istituto Nazionale di Astrofisica – Osservatorio Astronomico di Roma, Via Frascati 33, I-00040 Monte Porzio, Italy, e-mail: `menci@oa-roma.astro.it`

Abstract. I review the present status of galaxy formation models within a cosmological framework. I focus on semi-analytic models based on the Cold Dark Matter scenario, discussing the role of the different physical process involving dark matter and baryons in determining the observed statistical properties of galaxies and their dependence on cosmic time and on environment evolution. I will highlight some present problems and briefly present the main effects of assuming a Warm Dark Matter scenario.

Key words. Galaxies: formation

1. Introduction

The last decade has been characterized by a remarkable progress in the measurements of the galaxy properties over a huge range of cosmic times. Luminosity functions of galaxies have been measured up to $z \approx 8$ (Bouwens et al. 2011), showing a strong evolution, with a global star formation history peaking at $z \approx 2-3$ and rapidly decaying afterwards, especially in massive galaxies (for a review see Madau & Dickinson 2014); the size of galaxies shows an increase with cosmic time (a factor ~ 3 from $z = 2$ to $z = 0$ for spheroid-like objects), as well as the stellar content of galaxies (see, e.g., Fontana et al. 2006) growing on average by a factor ~ 10 from $z = 2$ to $z = 0$; morphological evolution has also been observed (see, e.g., Conselice 2014, for a review). Analogous observational progress involves the properties of local galaxies; e.g., the colors of the local galaxy population are observed to be characterized by a bimodal distribution, with massive galaxies belonging to a population of red objects with predominantly old stellar populations, clearly distinct from the blue star-forming galaxies with younger stellar populations, dominating the low-mass population (see Baldry et al. 2004). Such a bimodal distribution is also observed to depend strongly on environment, with the blue fraction of low-mass galaxies strongly decreasing in dense environments (Balogh et al. 2004).

All the above properties call for a physical theory of galaxy formation within a cosmological context. Since the matter content of the Universe is dominated by Dark Matter (DM, see, e.g., Planck Collaboration et al. 2014), such a theory must necessarely connect the gravitational processes dominated by DM to the physical processes affecting the baryonic component (gas, dust, stars). The early works in the early 90's (see, e.g., White & Frenk 1991) have stimulated a large number of groups which are contributing to develop an "ab initio" theory of galaxy formation (see Somerville & Davé 2015, for recent reviews), starting from the "seeds" provided by the tiny perturbations in the primordial density field. The power spectrum of such perturbations,

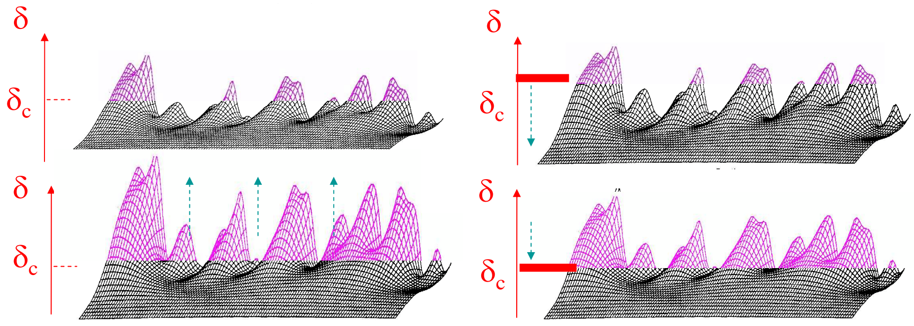

Fig. 1. Left Panel. A representation of a density field characterized by stochastic perturbations with a variance inversely dependent on their size (or mass scale). The field grows like $D(t)$ due to gravitational instability (top and bottom panels refer to times t_1 and t_2 with $t_2 > t_1$). Perturbations on larger and larger scales progressively cross the threshold and collapse. Right Panel: The same process can be represented keeping the density field as constant and adopting a threshold $\delta_c(t) \propto D(t)^{-1}$.

measured in detail through the anisotropies in the cosmic microwave background, has been shown to be consistent with that predicted by the Cold DM scenario from scales $r \sim 1$ Gpc down to $r \sim 10$ Mpc (Tegmark & Zaldarriaga 2002). Within such a cosmological framework, theoretical studies are based mostly on two approaches: i) hydrodynamical N-body simulations, which solve numerically the equations of motion of a system of N particles (representing the DM) under the influence of their mutual gravitational forces. The evolution of the particles simulating the gaseous component is described by numerically integrating the corresponding hydrodynamical equations. Sub-grid processes (like star formation) are described through specific recipes that connect them to the properties of the gas (like the density and the velocity field). While simulations allow to investigate the internal structure of galaxies and their spatial distribution, they require a significant computational effort to investigate the statistical properties of the galaxy population. ii) semi-analytic models (SAMs). They compute the collapse of DM condensations over progressively larger scales starting from the power spectrum, and connect the physical processes affecting the gas through simplified analytical descriptions relating the behaviour of the baryonic component to the depth of the dark matter potential wells. Although they do not provide a description of the spatial distribution of galaxies, their low computational cost makes them a powerful tool to investigate the statistical properties of galaxies when different prescriptions are adopted for the involved physical processes. The latter property makes them an ideal didactic tool to illustrate the physics involved in galaxy formation, so in the following I will concentrate on SAMs. As a consequence, I will focus mainly on the effect of the different processes involved in galaxy formation on the statistical properties of the galaxy population.

In sect. 2 I review the statistical description of the collapse and growth of DM halos from primordial density field, and the dynamics of sub-halos. In sect. 3 I discuss the physical properties affecting the gas and the star formation within DM potential wells. The basic structure of SAMs is briefly summarized in sect. 4. In sect. 5, the above theoretical framework is compared with existing observations, to discuss our present understanding of the

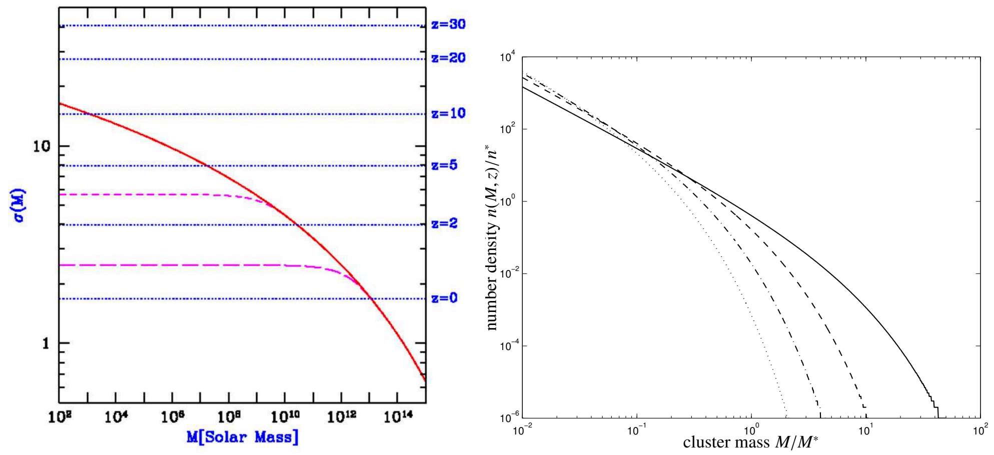

Fig. 2. Left panel: The variance $\sigma(M)$ of the density perturbation field is plotted as a function of the mass scale M for a CDM cosmology. Different thresholds for collapse are shown for different redshifts (see text). At a given redshift z, the mass corresponding to the intercept of the threshold with $\sigma(M)$ defines the typical mass scale $M_c(z)$ for the collapse. Right Panel: The Press & Schechter mass function is shown as a function of mass (in units of the characteristic mass at present time $M_c(z = 0)$ at four different redshifts: z = 3 (dotted line), z=2 (dot-dahsed line), z=1 (dashed line), and z=0 (solid line).

physical origin of the properties of galaxies. Sect. 6 is devoted to some open problems and perspectives.

2. The evolution of DM halos

2.1. The collapse and growth of DM halos

Galaxy formation and evolution is driven by the collapse and growth of DM halos, which originate from the gravitational instability of overdense regions in the primordial density field (see Peebles 1993). This is a random, Gaussian field within the "concordance cosmology" (Planck Collaboration et al. 2014), for which we adopt round parameters $\Omega_\Lambda = 0.7$, total matter density parameter $\Omega_M = 0.3$ (with baryons contribution corresponding to $\Omega_b = 0.04$ and Hubble constant, in units of 100 km/s/Mpc, $h = 0.7$. The normalization of the spectrum is taken to be $\sigma_8 = 0.9$ in terms of the variance of the field smoothed over regions of 8 h^{-1} Mpc.

The initial density perturbations have values $\delta \sim 10^{-5}$ (measured from the cosmic microwave background), and their growth due to gravitational instability can be initially computed solving the equations for a collisionless gravitating fluid in the linear regime. This yields a linear growth factor $D(t, \Omega_0, \Omega_\Lambda)$ increasing like a power low ($D(t) \sim t^{2/3}$ in a critical $\Omega = 1$ Universe) or slower (with a standstill at $z < 1$ in the case of $\Omega < 1$). When they reach the non-linear regime $\delta \sim 1$ the perturbations detach from the surrounding field and rapidly collapse. In the case of spherical perturbations, the collapse can be described analytically. It turns out that at the moment of collapse to a singularity the linear theory would predict an overdensity $\delta_c = 1.686$ (in a critical Universe; the values for a flat Universe with a nonzero cosmological constant are given by, e.g., Eke et al. 1998).

The statistical properties of the density field are described by the linear power spectrum $P(k)$ of DM perturbations as a function of the wave number $k = 2\pi/r$, where the size r corresponds to the mass scale $M \simeq 1.2\,10^{12}\,h^2 \mathrm{M}_\odot\,(r/\mathrm{Mpc})^3$. The power spectrum - measured mainly through the anisotropies in the CMB - is consistent with the Cold Dark Matter (CDM) model (see, e.g., Tegmark & Zaldarriaga 2002, and references therein).

The associated variance on the mass scale M plays a key role in determining the mass-dependent collapse history of DM perturbations. It reads:

$$\sigma^2(M) = \int \frac{dk\,k^2}{2\,\pi^2}\,P(k)\,W(kr) \qquad (1)$$

and quantifies the rms amplitude of perturbations as a function of the mass scale M (here W is the top-hat window function, see Peebles 1993). For a CDM spectrum, σ is characterized by an inverse dependence on the mass enclosed by the perturbations. This implies that small-scale perturbations have - on average - larger amplitude (as illustrated in Fig. 1). Thus, when the perturbation field grows like $\delta \sim D(t)$, perturbations on small mass scales are the first to reach the threshold for collapse δ_c (a visualization of such a process is provided by Fig. 1, while the mass dependence of the CDM variance $\sigma(M)$ is shown in the left panel of Fig. 2).

An equivalent formalism treats the perturbation field as constant, and assumes a constant density field and a time dependent threshold $\delta_c(t) = \delta_c\,D(t)^{-1}$ (right panel in Fig. 1). For increasing time, the threshold lowers and larger and larger regions of the density field cross the threshold $\delta_c(t)$ and collapse (Fig. 2), eventually leading to the formation of galaxies, groups and clusters of galaxies. Since the variance (Fig. 2 left panel) represents the rms amplitude of perturbations at a mass scale M, the intercept of $\sigma(M)$ with the threshold corresponding to a redshift z defines the typical mass scale $M_c(z)$ that collapses at the epoch corresponding to z (see Fig. 2 left panel).

The number density of virialized structures of mass M at the cosmic time t is given by the Press & Schechter (1974) expression:

$$N_H(M,t) = \sqrt{\frac{2}{\pi}}\,\frac{\rho_0}{M^2}\left|\frac{dln\sigma}{dlnM}\right|\frac{\delta_c(t)}{\sigma(M)}\,e^{-\frac{\delta_c^2}{2\sigma^2(M)}} \qquad (2)$$

where ρ_0 is the cosmic average matter density and $\sigma(M)$ is the rms density fluctuations in eq. (1). The above mass distribution is plotted in Fig. 3. At given redshift, it is characterized by a steep power law $N \sim M^{-1.8}$ at low masses, while at large M it shows a smooth exponential cutoff $N \sim exp(-M^{0.6})$. The characteristic mass $M_c(t)$ (the typical mass collapsing at a given cosmic time t illustrated in Fig. 1) separating the two regimes evolves with time ($\propto (1+z)^{-6}$ in a critical Universe). Note that the low-mass normalization decreases at the faint end, implying that with increasing cosmic time the number density of low-mass halos decreases to build up larger halos with mass $M \gtrsim M_c(t)$. Since $M_c(z=0) \approx 10^{15}\,M_\odot$, so that the present cosmic time is characterized by the collapse of large galaxy clusters.

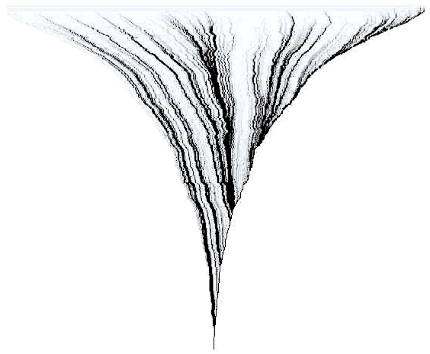

Fig. 3. A merger tree computed from the SAM in Menci et al. (2006) for a final halo mass $M = 10^{12}\,M_\odot$. Redshift ranges from $z = 0$ (bottom) to $z = 8$ (top). The thickness of each branch represents the mass of the corresponding halo.

Using canonical statistical tools it is possible to compute the probability that a halo collapsing at the mass scale M at time t, includes a perturbation that collapsed on a smaller mass scale M' at a previous time t'. This is given by the following expression (see Lacey & Cole 1993):

$$\frac{dP}{dM'}(M',t'|M,t) = \frac{\delta_c(t')-\delta_c(t)}{(2\pi)^{1/2}(\sigma'^2-\sigma^2)^{3/2}}\,\frac{M}{M'}\left|\frac{d\sigma'^2}{dM'}\right| e^{-\frac{[\delta_c(t')-\delta_c(t)]^2}{2(\sigma'^2-\sigma^2)}} \qquad (3)$$

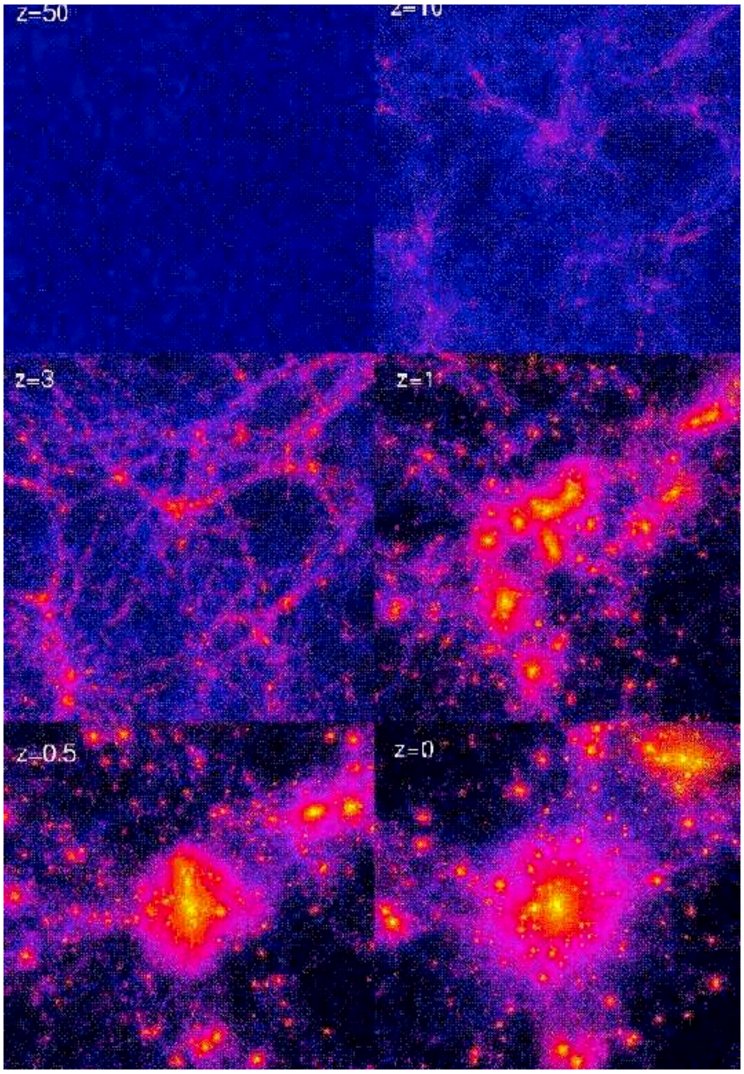

Fig. 4. The hierarchical evolution of a galaxy cluster in a universe dominated by cold dark matter in a snapshot of an N-body simulation (image courtesy B. Moore). Small fluctuations in the mass distribution constitute the seeds of cosmic structures. These grow by gravitational instability, merging and accretion of mass, eventually collapsing into virialised quasi-spherical dark matter halos. The colors represent the local density of dark matter plotted using a logarithmic colour scale. Linear overdensities are darker blue, whereas the non-linear collapsed regions attain over-densities of a million times the mean background density and are plotted as yellow/white. Each box is 10 Mpc on a side and the final cluster virial radius is 2 Mpc.

where σ and σ' are the rms density fluctuations corresponding to the masse M and M', respectively.

Based on the above progenitor mass distribution it is possible to reconstruct the merging histories of a given final DM halo mass (see, e.g., Somerville & Kolatt 1999; Cole et al. 2000). One example of such a "merging tree" is shown in Fig. 3 for a final halo mass $M = 10^{12}\,M_\odot$ (the halo of a Milky Way-like galaxy). Note that the number of major merging (mass ratio $M'/M > 0.2$) is much smaller than that of minor mergers, with the former mainly taking place at high redshifts $z \gtrsim 3$. At low redshifts the halo grows mainly through the accretion of much smaller lumps.

2.2. The dynamics of sub-halos

Here, we discuss the fate of sub-halos, i.e., the DM halos that have been included into a larger DM halo along one of the merging histories described above. After a time Δt from their inclusion, such sub-halos may i) sink to the centre due to the loss of angular momentum following dynamical friction; ii) merge with other galaxies due to random encounters. If the timescale for the above processes is longer than Δt, the sub-halos survive as satellite galaxies. To compute the time scale for processes i) and ii) we treat them in turn.

2.2.1. Dynamical friction

A sub-halo with mass m loses orbital angular momentum due to dynamical friction to the halo material when included into a host halo with mass M, and sinks to the centre. The timescale of such process is usually determined from the Chandrasekhar formula as given in Cole et al. (2000):

$$\tau_{df} = \Theta\ \tau_{dyn}\,\frac{0.3722}{ln(M/m)}\,\frac{M}{m}\ . \qquad (4)$$

Here $\tau_{dyn} \equiv R/V$ is the dynamical time of the halo, and $\Theta = [J/J_c(E)]^{0.78}\,[r_c(R)/R]^2$ contains the dependence on the initial energy E and angular momentum J of the galaxies, in terms of the angular momentum J_c and the radius r_c of the circular orbits corresponding to E. The values of Θ are statistically distributed approximately following a lognormal function with $\langle log_{10}\Theta\rangle = -0.14$ and $\langle(log_{10}\Theta - \langle log_{10}\Theta\rangle)^2\rangle^{1/2} \approx 0.26$ (see Tormen 1997). Note that for large M/m ratios one obtains $\tau_{df} \gg \tau_{dyn}$; such a long survival time of galaxies in massive halos is at the origin of the accumulation of a large number of galaxies within galaxy clusters. On the other hand, at high redshifts the smaller average M/m ratios (due to the larger frequency of major mergers discussed above) yields a rapid coalescence of sub-halos with the central galaxy, so that high-redshifts host halos have - on average - small occupation numbers compared to low-redshifts large mass halos.

2.2.2. Merging following random encounters

The average rate for binary aggregations between clumps with mass m and m' (and corresponding radius r and r') is:

$$\tau_{agg}^{-1} = \frac{\epsilon(V_{rel})\,V_{rel}}{4\pi R^3/3}\ \pi\,(r^2 + r'^2)\Big(1 + \frac{G}{V_{rel}^2}\,\frac{m + m'}{r + r'}\Big) \qquad (5)$$

where the average is over the relative velocities V_{rel} and $\epsilon(V_{rel})$ is an efficiency which depends inversely on V_{rel}^2 (Saslaw 1985). The average value for relative velocity is $V_{rel} = V_c/\sqrt{2}$ where V_c is the host halo circular velocity. This means that in massive halos the binary merging rate is inefficient due to the large relative velocities of sub-halos. On the other hand, the aggregation rate is strongly enhanced for encounters between clumps with comparable mass. Such conditions favor aggregations due to random encounters at high redshifts, due to the lower host halo circular velocity (with corresponding smaller values of V_{rel}) and to the larger number of sub-halos with comparable mass (see sect. 2.1).

2.3. Hierarchical structure formation

To summarize what presented above, we refer to Fig. 4 which includes different snapshots of an N-body simulation of the formation of a galaxy cluster. This illustrates the collapse of perturbations on progressively larger scales and the dynamical evolution of the sub-clumps included into larger halos. At early cosmic times ($z = 50$, top left) only tiny density perturbations are present, with a power spectrum like that discussed in sect. 2.1. These grow due to gravitational instability. Since small scale

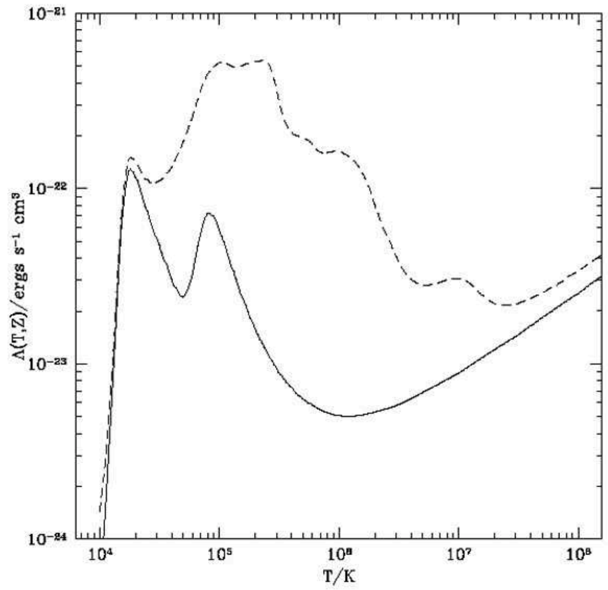

Fig. 5. Cooling functions for gas in collisional ionization equilibrium are shown as a function of temperature (Sutherland & Dopita 1993). The solid line corresponds to gas of primordial composition, while the dashed line corresponds to gas of Solar composition.

perturbations have - on average - larger amplitudes, these are the first to collapse to form galactic-size halos (panels 2-3 from top left). These initially do not contain sub-clumps since at high redshifts any substructure rapidly coalesce with the central object, as we discussed in Sect. 2.2.1 and 2.2.2. Later on, larger regions reach the threshold for collapse (panel 4) including previously formed halos (following what described in Sect. 2.1, Fig. 3 and Fig. 4). Due to the longer timescale for dynamical friction and aggregation (sect. 2.2.1 and 2.2.2), the sub-clumps now accumulate inside the host halo, to form the satellite galaxies of the final galaxy cluster (panel 6).

2.4. Non-linear evolution: spherical model

The final status of a collapsed and virialized perturbation can be followed through N-body simulations or through analytic simplified models. The simplest description is the spherical model, which assumes that – once reached the threshold for collapse – the perturbations detach from the Hubble flow and evolve like isolated spheres. In such case the final average density of the DM halo can be computed (Peebles 1993) and turns out to be $\overline{\rho} = 180\rho_0$ where ρ_0 is the background average density. The density profile inside the halo can also be worked out. Simulations have shown that the final profiles are steeper than those corresponding to a the simple isothermal case $\rho(r) \sim r^{-2}$, and can be fitted with a form $\rho(r)/\rho_{crit} = \overline{\delta}/(r/r_s)(1 + r/r_s)^2$, where ρ_{crit} is the critical density for closed Universe, $\overline{\delta}$ is a characteristic (dimensionless) density depending on the collapse redshift, and r_s is a scale radius weakly depending on the mass M of the collapsed halo (details can be found in Navarro et al. 1997). The typical size of DM halos is instead provided by the virial radius $R_v \approx (3M/4\pi\overline{\rho})^{1/3} \approx 8\,h^{-1}\mathrm{kpc}\,(M/10^9\,h^{-1}\,M_\odot)^{1/3}(\Omega/\Omega(z))^{-1/3}/(1+z)$.

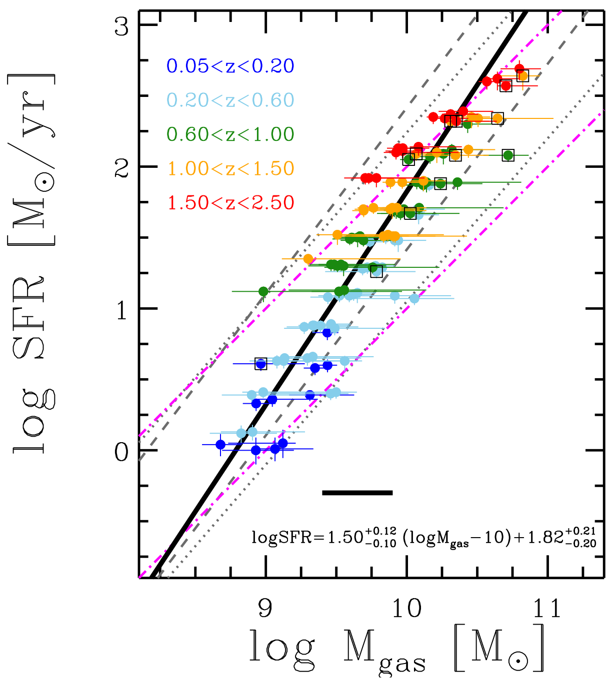

Fig. 6. Relation between SFR and gas mass. The colour code indicates different redshift intervals, as shown by the legend. The solid thick black line is the power law fit to all data, and the best-fit relation is reported in the lower right corner. Magenta dashed-dotted lines indicate constant star formation efficiency (i.e., constant depletion times) of 1 (lower curve) and 10 (upper curve) Gyr (from Santini et al. 2014)

3. Connecting the physics of baryons to the DM halos

The evolution of the DM halos is approximately scale-invariant. The larger and larger DM structure that form with increasing cosmic time are the scaled-up version of those formed at earlier times on smaller scales. However, the baryonic process taking place inside the potential wells of DM halos strongly depends on the depth of such potential wells, and hence on the DM mass of the halo. This is primary because baryons can radiate away their thermal energy E_{therm} due to emission processes, as we discuss next.

3.1. Gas cooling

When a halo collapses, this is initially filled with shock-heated gas at the virial temperature $T_v \sim k_b^{-1}\, GM/R_v$. In the simple isothermal case its density distribution $n(r) \sim \rho(r)^\beta$ is determined by the DM density distribution (sect. 2.4) through the ratio of DM to gas specific energies $\beta = \sigma^2_{DM}/k_b\, T_v/(\mu\, m_p)$ (where $\mu \approx 0.6$ is the mean molecular weight and m_p is the proton mass). Using the expression for the virial radius and for the average DM inner density described in sect. 2.4 yields:

$$T_v = 10^4\mathrm{K}\left(\frac{M}{10^9\, h^{-1} M_\odot}\right)^{2/3}\left(\frac{\Omega}{\Omega(z)}\right)^{1/6}(1+z) \quad (6)$$

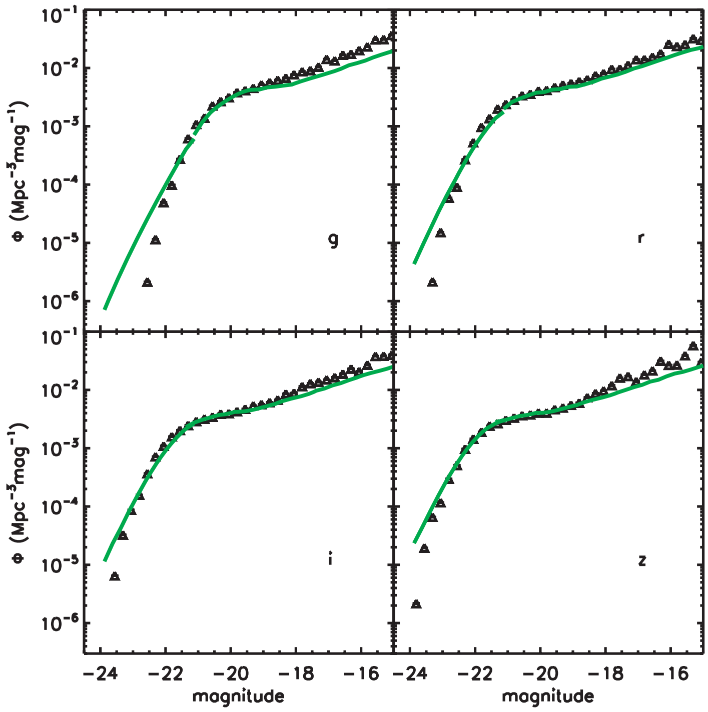

Fig. 7. Galaxy luminosity functions in the SDSS g, r, i and z photometric bands. The smooth green curves are predictions the Guo et al. (2011) SAM. The symbols are observational data for a low-redshift SDSS sample taken from Blanton et al. (2005).

The hot gas is subject to different atomic processes which cause it to radiate away part of its thermal energy. These are mainly collisional excitation/de-excitation (for $T \lesssim 10^7$ K) and bremmstrahlung (for larger T). Both processes depend n^2 where n is the number density of gas particles. The energy radiated per unit time (divided by n^2) is shown in Fig. 5 (cooling function $\Lambda(T)$). Since this is a strong function of T, the cooling efficiency of gas inside the DM potential wells depends on the mass M of the DM halo through eq. 6, being maximal for temperatures $\sim 2\,10^4 - 5\,10^6$ K (the excitation energy of H and He) corresponding to DM halos with $10^9 \lesssim M/M_\odot \lesssim 10^{13}$. For such halos the cooling time $t_{cool} \equiv E_{therm}/\Lambda(T)\,n^2$ is smaller than the Hubble time t_H, so that gas effectively cools. Note that for halos with mass $M \gtrsim 10^{13}\,M_\odot$ (groups and clusters of galaxies) the smaller values of the cooling function result into $t_{cool} > t_H$ (except in the very inner regions where the large gas density n can result into $t_{cool} < t_H$yielding a cooling flow).

Such a strong dependence of cooling on the mass of the DM halo breaks the self-similarity of cosmic structures. Gas inside galaxy-size halos effectively cools and flows to the centre.

3.2. The formation of Galactic disks

Since cooled gas is no longer supported against gravity by thermal pressure, it flows to the centre of the DM halo. Conservation of angular momentum J causes an increase of the angular velocity until the cooled gas reaches centrifugal equilibrium and settles into a rotationally supported disk (see Mo et al. 1998, for a detailed treatment). The size and the rotational velocity of the disk depends on the initial angular momentum of the DM halo (transferred to the gas). This is usually expressed in terms of the ratio $\lambda \equiv \omega/\omega_{rot}$ between the initial rotation $\omega = J/M\,R^2$ of the DM halo and the angular velocity that would correspond to a centrifugal equilibrium $R^2\,\omega_{rot} = G\,M/R^2$. This is known to be approximately distributed according to a log-normal distribution (see, e.g., Warren et al. 1992) peaking at a value $\lambda = 0.05$ (DM halos are mainly sustained against gravity by pressure rather than rotation). Such a small value implies that cooled gas must reach a very inner radius $r_d \approx \lambda\,R_{vir} \sim 2-5$ kpc before it acquires sufficient rotation to balance the DM gravity.

3.3. Secular star formation in Galactic disks

The cold gas mass m_{cold} in the disk constitutes the reservoir for star formation. Although at small-scales (compared to the total galactic sizes) star formation constitutes a complex phenomenon, it is well known that at galactic scales the global star formation rate is directly connected to the mass of the cold gas of the disk by the Kennicut-Schmidt relation $\Sigma_{SFR} \propto \Sigma_{gas}^{1.5}$ (Schmidt 1959; Kennicutt 1998). This can be recast in terms of a disk timescale $\tau_* \propto \Sigma_{gas}^{-1/2}$, to obtain a relation between the star formation rate (SFR) and the cold gas mass $\dot{m}_* = m_{cold}/\tau_*$ (see Fig. 6). Recent works have measured the star conversion timescale with increasing precision (Daddi et al. 2010; Genzel et al. 2010; Santini et al. 2014) finding $\tau_* \approx 1$ Gyr in the local Universe, slowly decreasing with time as to yield $\tau_*(z = 2) \approx 100$ Myr.

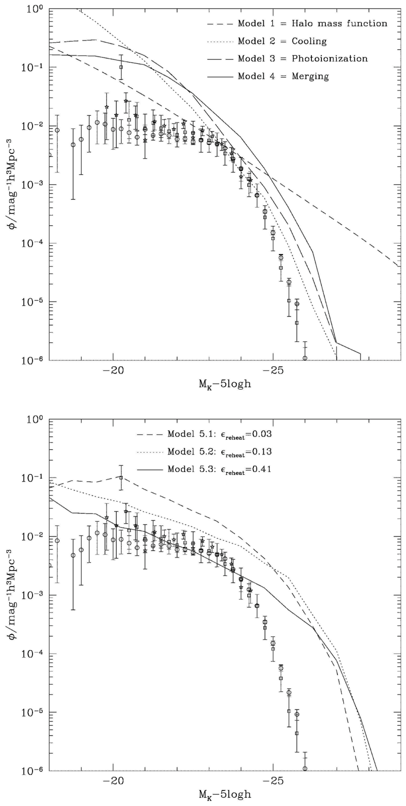

Fig. 8. Top Panel: The luminosity function of galaxies from the SAM in Benson et al. (2003, lines) is compared with observations by Cole et al. (2001, circles), Kochanek et al. (2001, squares), and Huang et al. (2003). The dashed line shows the result of converting the DM halo mass function into a galaxy luminosity function by assuming a fixed mass-to-light ratio chosen to match the knee of the luminosity function. The dotted line shows the result of including cooling in the model. Long-dashed and solid lines show the effects of adding reionization and galaxy merging, respectively. Bottom Panel: The same observations in the top panel are compared with SAMs with different values of the Supernovae efficiency (see sect. 3.5).

3.4. Impulsive star formation

Galaxy interactions (sect. 2.2) can trigger powerful starbursts over short timescales close to the galaxy interaction time $\tau_b \sim r_d/V_{rel} \sim 10^2$ Myr (see, e.g., Sanders & Mirabel 1996). Analytical models (Cavaliere & Vittorini 2000) and hydrodynamic simulations of binary galaxy mergers (e.g., Cox et al. 2008) have shown that the fraction of gas destabilized from the disk and converted into stars is a fairly strong function of the mass ratio of the merger m'/m. For major mergers with $m'/m \approx 1$ almost all the cold gas can be converted into stars over times $\lesssim$ 100 Myr yielding star formation rates up to $\sim 10^3\, M_\odot$/yr.

3.5. Supernovae feedback

Since the earliest studies of galaxy formation in hierarchically universes it appeared clear that a problem of the the above scenario can be constituted by overcooling (White & Rees 1978). In fact, the first objects to collapse are low-mass galaxies with $M \sim 10^8 - 10^9 M_\odot$ which are characterized by high density (sect. 2.4) and low virial temperature $T \sim 10^4 - 10^5$ K (eq. 6). Such conditions lead to an extremely efficient gas cooling (sect. 3.1) which constitutes a runaway process, since cold gas becomes denser thus enhancing the cooling rate. This would lead to an early conversion of gas into cold gas and stars which would not leave any cold gas left at low redshift in the galaxies that formed later on, in conflict with what we observe. The solution to this problem is constituted by the energy feedback onto the gas by the Supernovae which follow the star formation (see Dekel & Silk 1986). The total energy dumped into the gas by the collective effect of Supernovae following the formation of a stellar mass Δm_* can be estimated as $E_{SN} \approx 10^{51}\, \eta_{IMF}\, \epsilon_0\, \Delta m_*$ erg, where $\sim 10^{51}$ erg is the energy released by a single type II Supernova, $\eta_{IMF} \sim 1 - 5\, 10^{-3}/M_\odot$ is the number of type II Supernovae per solar mass of stars (depending on the IMF), and $\epsilon_0 = 0.01 - 0.1$ is an efficiency determining the fraction of energy actually dumped into the interstellar medium. Such an energy can be compared to the gravitational energy $\sim \Delta M_{gas}\, V_c^2$ of a gas mass ΔM_{gas} in the galaxy potential wells. The mass of ejected gas can then be estimated as $\Delta M_{gas} = \Delta M_*\, E_{SN}/V_c^2$. This shows feedback can effectively balance star formation ($\Delta m_{gas} \sim \Delta m_*$) in low-mass galaxies with circular velocity with $V_c \lesssim 100$ km/s.

3.6. Other processes affecting the gas and stellar content of galaxies

Recent SAMs include additional processes affecting the gas and stellar content of galaxies. These include:

i) The suppression of cooling in small DM halos due to the effect of the UV background. This inhibits the formation of a cold gas component and hence of star formation in low mass DM halos with circular velocities below $V_{reion} \approx 50$ km/s after redshift $z \approx 6$ (see Benson et al. 2002, 2003, for detailed calculation).

ii) The stripping of stars and gas in satellite galaxies due to the tidal effect of the gravitational potential of the host halo. For each satellite galaxy, the tidal radius is identified as the distance from the satellite centre at which the radial forces acting on it cancel out (King 1962; Binney & Tremaine 1987). These forces are the gravitational binding force of the satellite, the tidal force from the central halo and the centrifugal force. In the simple approximation of nearly circular orbits and of an isothermal halo density profile, such a radius can be expressed as $r_t \approx \sigma_{sat}\, r_{sat}/\sqrt{2}\, \sigma_{halo}$, where σ_{sat} and σ_{halo} are the velocity dispersions of the satellite and of the halo, respectively, and r_{sat} is the halocentric radius of the satellite, that are computed in SAMs following the decay of satellite orbits to the centre due to dynamical friction. For each satellite galaxy, the material outside this radius is assumed to be disrupted and becomes a diffuse stellar component in the host halo (see Henriques & Thomas 2010).

iii) The stripping of the gas in satellite galaxies due to the ram pressure of the intergalactic plasma in the host halo. For a galaxy moving with velocity v at a distance r from the centre of a halo, the condition for gas stripping is $\rho_h\, v^2 \geq 2\,\pi\, G\, \Sigma(r)\Sigma_g(R)$, where ρ_h is the density of the diffuse plasma in the host halo, and Σ and Σ_g are the stellar and gas surface density, respectively. Note that when applied to the cold gas component of host galaxies, the large density avoids appreciable stripping, while for the hot gas component with much lower density (a factor $\sim 10^{-3}$) the gas is efficiently stripped off. For such a reason, most SAMs simply assume that the hot gas component is instantaneously stripped when galaxies become satellites in a host halo (though same models adopt a refined treatment, see, e.g., Guo et al. 2011).

3.7. Stellar populations

The emission properties of galaxies can be derived from stellar population models. These provide the spectral energy distribution $S_\lambda(t-t')$ at time t for different wavelengths λ due to a population of stars formed (with a given IMF) in a single burst at time t' (see, e.g., Bruzual & Charlot 2003). For small $t-t'$ values, and for $t' \leq 1$ Gyr, $S_\lambda(t-t')$ peaks at short wavelengths due to the strong UV emission from massive, short-lived stars, while for increasing ages $t-t'$ the spectra become redder due to the contribution of old stars. To describe the stellar populations in galaxies evolving in a cosmological framework, the single-burst emission must be convolved with the star formation rate $\dot{m}_*$ of all populations that formed during the history of a galaxy and of its progenitors. The overall spectral emission is thus given by

$$L_\lambda(t) = \int_0^t S_\lambda(t-t')\, \dot{m}_*(t'). \tag{7}$$

3.8. Black hole accretion and AGN feedback

State-of-the-art SAMs also include a description of the growth of supermassive Black Holes (BHs), that observations show to be hosted at the centre of most local galaxies (see Richstone et al. 1998). It is now widely accepted that the formation and the evolution of such BHs is strongly correlated with that of the host galaxies, due to the observed tightness of the relations between the BH mass and the galaxy properties such as the stellar mass or the velocity dispersion of the bulge (see Kormendy & Ho 2013, for a review). Together with the observed low fraction of Active Galactic Nuclei (AGN) and with the strong cosmological evolution of the number density of bright AGNs (for a review see Merloni & Heinz 2013), such

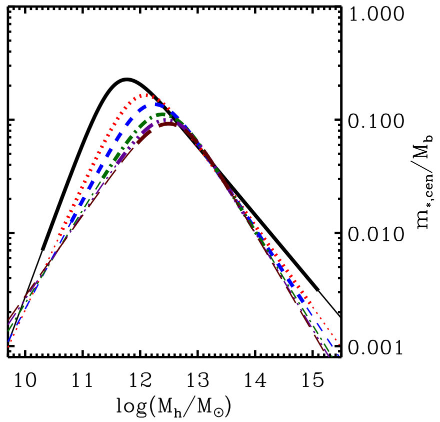

Fig. 9. Median stellar mass assembly efficiency plotted as a function of halo mass (from Moster et al. 2013) at $z = 0$ (solid line) to $z = 0.5$ (dotted), $z = 1$ (short dashed), $z = 2$ (dot-dashed), $z = 3$ (three dots-dashed), $z = 4$ (long dashed).

measured relations strongly indicate that a major fraction of the BH mass results from accretion of gas during relatively short (duration $\tau \approx 10^7$ yrs) but intense (accretion rates $\dot{M}_{BH} \approx 1\div 10\, M_\odot$/yr), repeated bursts (see, e.g., Shankar et al. 2009). During such episodes, a considerable fraction of the energy emitted by AGNs is injected into the galactic gas (see Fabian 2012, for a review).

Present SAMs provide different descriptions to connect the BH accretion to the properties of the host galaxy, mostly assuming galaxy interactions and disk instabilities to drive the accretion events (see Menci et al. 2006; Croton et al. 2006; Hirschmann et al. 2012). All the different descriptions are calibrated as to yield final BH masses M_{BH} matching the observed local correlations with the properties of the host galaxies. The AGN emitted energy $L = \eta\, c^2\, \dot{M}_{BH}$ resulting from the BH accretion (with an energy-conversion efficiency $\eta \approx 0.1$, see Yu & Tremaine 2002) is then assumed to be partially transferred to the galactic gas, with an efficiency $f_{AGN} \approx (m_p\, v^2/2)/h\, \nu$ determined by the gas particles to photon energy ratio. The latter can be estimated assuming momentum transfer from photons to gas $m_p\, v = h\, \nu/c$, which yields $f_{AGN} \approx v/2\, c$. For gas outflow

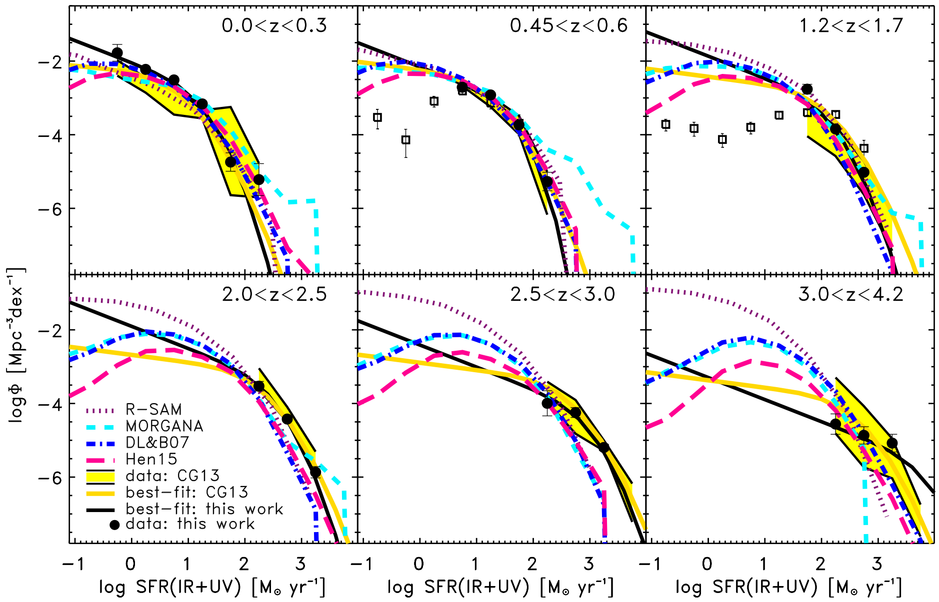

Fig. 10. The distribution of star formation rate measured through the IR+UV emission) in six redshift bins (Gruppioni et al. 2015). The black solid line represents the best fit to the data with a modified Schechter function, while the yellow solid line is the distribution derived from the total IR luminosity function (without excluding AGN contribution through SED decomposition). The data from of 24 μm sources with $log(M/M_{\odot}) > 10$ in the GOODS-S by Fontanot et al. (2012) are plotted for comparison as black open squares. The SAMS predictions are shown as purple dotted (Menci et al. 2014), sea-green short-dashed (Monaco et al. 2007), blue dot-dashed (De Lucia & Blaizot 2007) and deep-pink long-dashed (Henriques et al. 2015) coloured lines.

velocities $c \sim 0.1$ (observed through absorption lines in the X-ray emission of AGNs, see Crenshaw et al. 2003; Chartas et al. 2002) we obtain $f_{AGN} \approx 0.05$. Such a coupling factor is sufficient to heat and eject most of the gas during the AGN phase following a major merger. In addition to the above "Quasar Mode" of feedback, tightly related to the strong AGN phase, some models include the continuous energy injection associated to a "low accretion state" (low Eddington ratios $< 10^{-3}$) of BHs. Such a "Radio Mode" of feedback is often associated with the cavities observed in X-ray images of hot gas in galaxy clusters (see Fabian 2012, for a review).

The large feedback efficiency $f_{AGN} \approx 1$ assumed to be associated with the Radio Mode yields feedback energies able to effectively reduce the gas cooling described in sect. 3.1 (see Croton et al. 2006).

4. Semi-analytic models of galaxy formation

Based on the processes described above, semi-analytic models (SAMs) connect the evolution of the DM halos presented in sect. 2 to the baryonic processes illustrated in sect. 3, to provide a description of the galaxy population derived "ab initio" in a cosmological framework. Here briefly summarize the key steps adopted by most SAMs.

1. A time grid is set between an initial time t_i (corresponding to a chosen large redshift $z \gtrsim 10$) to a final time t_0 corresponding to $z = 0$.

2. A set of DM parent halo masses M is considered at t_0; these are distributed according to the mass function in eq. (2).

3. A Monte Carlo procedure is used to extract the progenitors of each parent halo at previous times along the grid (down to an initial time t_i) on the basis of the progenitor distribution eq. (3). The procedure is repeated to generate a number of merger trees like that shown in Fig. 3.
4. For each time step starting from the initial time t_i, the sub-halos included in a larger halo in a given time step are considered. For each of them the merging with the central galaxy or with another satellite galaxy is computed through the merging rates described in sect. 2 (eqs. 4 and 5). This allows to generate a full catalogue of halos and sub-halos (corresponding to a galaxy) at each time step, keeping track of the merging events associated to each galaxy.
5. Starting from the initial time t_i, the baryonic processes described in sect. 3 are computed for each DM clump during a time-step Δt.
   (a) Gas Cooling, described in sect. 3. The cooling radius is computed as the region enclosing a gas density $n(r)$ high enough to yield a gas cooling time $E_{therm}/n^2(r_{cool})\,\Lambda(T_V)$ smaller than the lifetime of the halo. The mass of cooled gas (enclosed within r_{cool}) is then assigned to a disk with radius r_d as described in sect. 3.2.
   (b) The star formation rate, associated to the secular conversion of cold gas, is computed as described in sect. 3.3.
   (c) When galaxies merge, the associated starbursts are computed as described in sect. 3.4. In the case of major mergers (typically when the mass ratio of the merging partners is $m'/m \gtrsim 0.2$, see Khochfar & Silk 2006; Parry, Eke & Frenk 2009) the stellar mass in the disk is transferred to a bulge.
   (d) The re-heating of part of the cold gas due to the energy feedback by Supernovae following star formation. The re-heated gas mass Δm_{gas} is computed as described in sect. 3.5 and the cold gas mass m_c is decreased by a corresponding amount.
   (e) The emission from the stellar populations in different bands is computed by tracking back and convolving the star formation histories of all progenitors of galaxies with spectral energy distributions from population synthesis models, as described in sect. 3.7.
   (f) A BH accretion rate is computed in case of galaxy merging, or when the galactic gas mass exceeds the threshold for the onset of disk instability (see references in sect. 3.8). The energy injected into the gas due to AGN feedback is computed as $\Delta E_{AGN} = f_{AGN}\,\eta\,c^2\,\dot{M}_{BH}$ (sect. 3.7). The corresponding ejection of galactic gas is either assumed to counteract the cooling rate at point a) (e.g., Croton et al. 2006) or to induce the expansion of blast waves that eject part of the cold gas mass Δm_c (e.g., Menci et al. 2008).

6. The procedure is iterated from step 4 until the final time ($z = 0$) is reached.

Note that the SAMs allow also to compute the growth of galactic bulges during major mergers. After such events, if a gas reservoir is still available, further gas cooling will lead to the formation of a new disk around the bulge. The above procedure allows to obtain a simulated catalogue of galaxies, each with the following computed quantities: DM halo mass M (and hence circular velocity V_c, virial temperature T_v and radius R_v), DM density profile $\rho(r)$, cold disk gas m_{cold}, disk size r_d, star formation rate $\dot{m}_*$ and stellar content m_* (obtained integrating the $\dot{m}_*$ contributed by all progenitors), fraction of stellar mass in the bulge (B/T ratio), emission L_λ from all the stellar populations. In addition, including proper models connecting the disk gas mass to the dust content of galaxies (see, e.g., Granato et al. 2000) allows to compute the absorption properties of each galaxy.

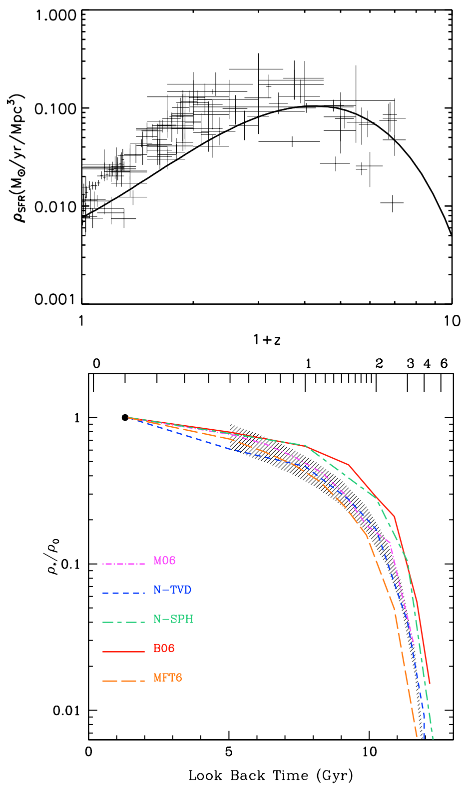

Fig. 11. Top Panel. The evolution of the cosmic SFR: data are from Li & White (2009) while the line shows the prediction of the SAM in Guo et al. (2011). Bottom Panel. Comparison between the observed Stellar Mass Density (in galaxies with $m_* \geq 10^{11}\,M_{\odot}$, Fontana et al. 2006, shaded area) and the corresponding predictions by recent theoretical models, as a function of redshift: (Menci et al. 2006; Monaco et al. 2007; Nagamine et al. 2005a,b, M06, MFT06, N-TVD, N-SPH, respectively).

5. Comparisons with observations

In this section we compare the predictions of different SAMs with existing observations, to single out the main physical processes responsible for the observed properties of the galaxy population.

5.1. The DM and baryonic processes shaping the local luminosity function

Present SAMs based on the above approach (sect. 4) can provide excellent fits to the local luminosity function of galaxies. An instance is shown in Fig. 7, taken from Guo et al. (2011, similar results are obtained by other SAMs).

The role played by the different processes described in sects. 2 and 3 is apparent in Fig. 8 (from Benson et al. 2003). While the mass function of DM halos (eq. 2) is characterized by a steep power law $\sim M^{-1.8}$ at small masses, and by a smooth exponential cutoff $exp(-M^{0.6})$ at large M (see sect. 2.1), the observed galaxy luminosity function are characterized by a Schechter form $N(L) \sim L^{-1.2}\,exp(-L)$, with a much flatter power law and a steeper cutoff. A first modification of the halo mass function (dashed line in Fig. 8) is provided by the merging of sub-halos associated to single galaxies as described in sect. 2.2 (solid line). However, even the sub-halo mass function is too steep at the low-mass end and too extended at the high mass end.

Thus, the baryonic processes must strongly suppress the L/M ratio at both the faint and the bright end of the distribution. At the faint end, the suppression of the L/M ratio is due to the efficiency of feedback in depleting the cold gas reservoir of low-mass halos discussed in sect. 3.5 (bottom panel in Fig. 8). An additional suppression is provided by the effect of photo-ionization from the UV background (see sect. 3.6 point i).

At the bright end, such a suppression is due to the inefficient cooling in massive halos discussed in sect. 3.1 (left hand panel in Fig. 8). Note that the L/M suppression at the bright end due to the inefficient cooling is not sufficient to cause the excellent match apparent in Fig. 7. This is due to the fact that a fraction of the gas in large mass halos has previously cooled inside smaller progenitor halos. Thus, in recent SAM like that shown in Fig. 7, the additional suppression is provided by the AGN feedback described in sect. 3.7.

The above considerations for the L/M ratio, suppressed for both small and large halo masses M as described above, imply that star

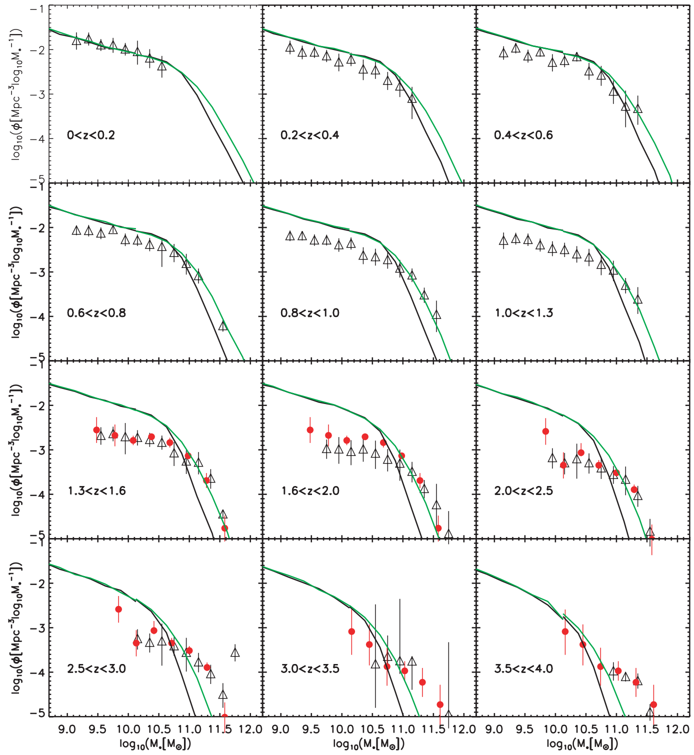

Fig. 12. Stellar mass functions at different redshifts. Data are taken from Pérez-González et al. (2008, triangles) and from Marchesini et al. (2009, filled circles). Black curves are the functions measured directly from the SAM, while green curves show the result of convolving the predictions with a Gaussian of dispersion 0.25 dex in *logM* in order to represent uncertainties in the individual observational stellar mass determinations (from Guo et al. 2011).

formation of stars reaches a maximal efficiency at intermediate scales $M \sim 10^{12}\, M_{\odot}$ characteristic of local spiral galaxies, as shown in Fig. 9 (from Moster et al. 2013).

5.2. What drives the evolution of galaxies

The distribution of the galaxy star formation rate (SFR) at different cosmic epochs from different SAMs is shown in Fig 10 and compared with the data. Note that all models provide similar predictions, and agree with the data in showing an increase of the average SFR from $z = 0$ to $z = 3$. This suggest a scenario in which a rapid phase characterized by high SFR at $z \gtrsim 3$ is followed by the decline of star formation especially in massive galaxies (large SFR). Such a two phase scenario is well illustrated by the evolution of the cosmic SFR (the total SFR in galaxies per Mpc^3) and global stellar mass density (the total stellar mass in galaxies per Mpc^3) shown in Fig. 11.

The above behaviour can be traced back to the DM and baryonic processes described in sect. 2 and 3. At high redshifts $z \gtrsim 3$, the large densities attained by DM and gas within DM halos (sect. 2.4) and the small virial temperatures characterizing the first low-mass halos (sect. 2.1 and eq. 5) yield rapid gas cooling

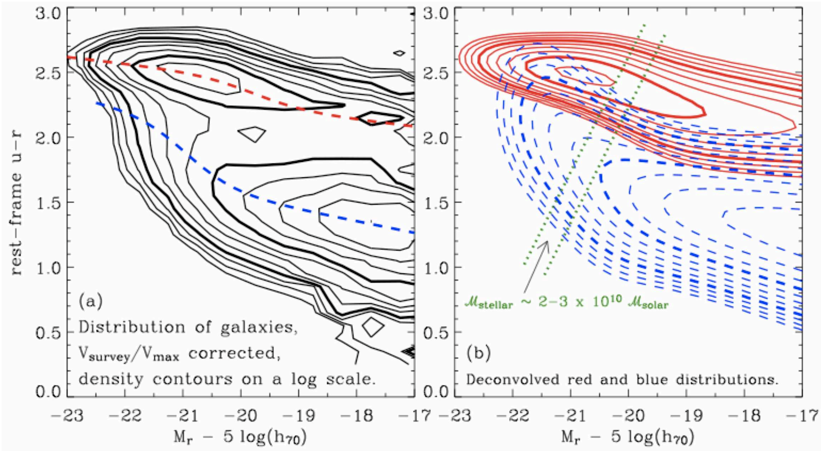

Fig. 13. The contours are the density of SDSS galaxies (in log scale, doubling every two levels) in color-luminosity space. The dashed lines are the mean relations of the red sequence and blue cloud, respectively (Baldry et al. 2004).

(sect. 3.1). The small dynamical timescales and the high rate of major merging of DM halos (sect. 2.1, 2.2, and 2.3) cause the efficient and rapid conversion of gas into stars (3.3 and 3.4), contributing to the rapid growth of the cosmic SFR (Fig. 10 and Fig. 11a) and of the stellar mass density (Fig 11b). When halos grow, the larger virial temperatures cause a decrease of the cooling time (sect. 3.1), while the frequency of starbursts (sect. 3.3) drops due lower rate of interactions (sect. 2.1-2.3). Such a decrease of the cooling and star formation efficiency, together with the gradual exhaustion of gas, results in the decline of the star formation rate shown in Fig. 10 and Fig. 11.

An important issue is constituted by the over-prediction of the abundances of low-SFR galaxies at $log(\dot{m}_*/M_\odot/yr) < 1$, becoming more and more important with increasing redshift. This constitutes an instance of a the well-known excess of low/intermediate mass galaxies at $z \gtrsim 1$ predicted by most SAMs with respect to observed mass functions (see, e.g., Somerville & Primack 1999; Cole et al. 2000; Menci et al. 2002; Croton et al. 2006; Guo et al. 2011) illustrated by the stellar mass function shown in Fig. 12 (from Guo et al. 2011). This is due to the fact that at high redshifts the large densities of DM clumps (sect. 2.4) result into large DM circular velocities even in small mass halos. This decreases the effectiveness of feedback in suppressing the star formation in low-mass halos (sect. 3.5) so that the steep slope of the DM halo mass function - not balanced by feedback - results into an exceedingly large number of low-mass galaxies. This aspect is a result of the small-scale power excess typical of the CDM power spectrum (e.g. Klypin et al. 1999; Moore et al. 1999).

5.3. What drives the color distribution of galaxies and the downsizing

The color of galaxies is characterized by a bimodal distribution (see Fig. 13). On the one hand, massive, luminous galaxies populate the "red sequence", mainly constituted by old, passively evolving stellar population and by small gas fractions. On the other hand, small mass galaxies largely contribute to the "blue cloud" which is constituted by star forming, gas rich galaxies. Such and inverse order in the star formation epoch with increasing galaxy mass is sometimes referred to as "downsizing".

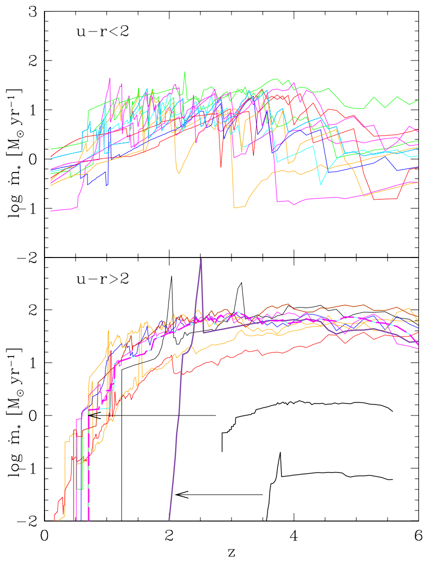

Fig. 14. Star formation histories drawn from the SAM in Menci et al. (2006). Each curve represents the sum of the $\dot{m}_*$ in all the progenitor clumps (at any given z) of galaxies belonging (at $z = 0$) to the blue ($u{-}r < 2$, top panel) and to the red ($u{-}r > 2$, bottom panel) populations. Two star formation histories relevant to our discussion (see text) are highlightened by heavy curves (solid and dashed) and evidenced by the insets in the lower part of the plot.

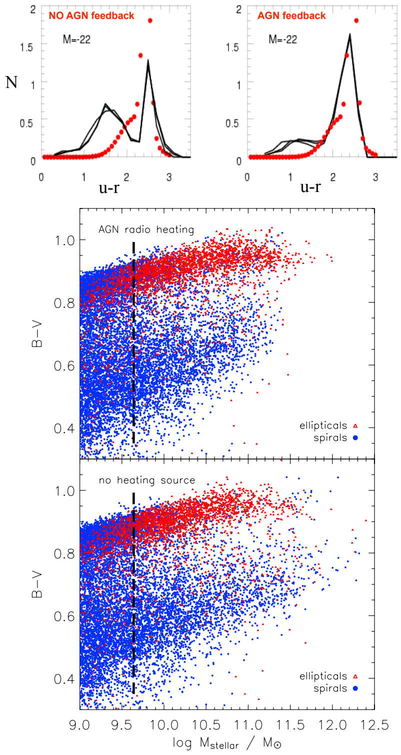

Fig. 15. Top Panel. The rest-frame $u - r$ color distributions in the SAM by Menci et al. (2006, heavy lines) for different dust extiction laws are compared with the Gaussian fit to the SDSS data (from Baldry et al. 2004, dote) for bright $M_r = -22$ galaxies. The left column refers to the model without AGN feedback, while right column shows the results when AGN feedback is turned on. Bottom Panels. The predicted color-magnitude distribution from the SAM by Croton et al. (2006) with (bottom) and without (top) AGN feedback.

The origin of such a bimodality can be traced back to the mass dependence of the evolutionary behavior presented in the previous section. In such a context, a correlation between the galaxy mass and the color is naturally predicted. In fact, the progenitors of massive galaxies are formed from the collapse of small-scale DM fluctuations which are on top of a larger scale density perturbation. Thus star formation in progenitor clumps of the massive galaxies is peaked at higher redshift compared to that taking place in progenitors of small-mass galaxies, since the former form in the biased, high-density regions of the density field, collapsing at higher z and containing denser gas. This leads to star formation characterized by larger SFR at high at z. In turn, this results into the early conversion of gas into stars leaving little or no gas reservoirs for later star formation, thus originating a population of red passive objects. The progenitors of low-mass galaxies form in lower-density regions of the perturbation field, and start to form stars later on, leaving abundant gas left over for star formation at low redshifts. Some instances of such star formation histories are shown in Fig. 14.

Although the above ”biasing” effect can partially explain the observed color-magnitude distribution of galaxies, in all SAM models it is not sufficient to provide the observed ex-

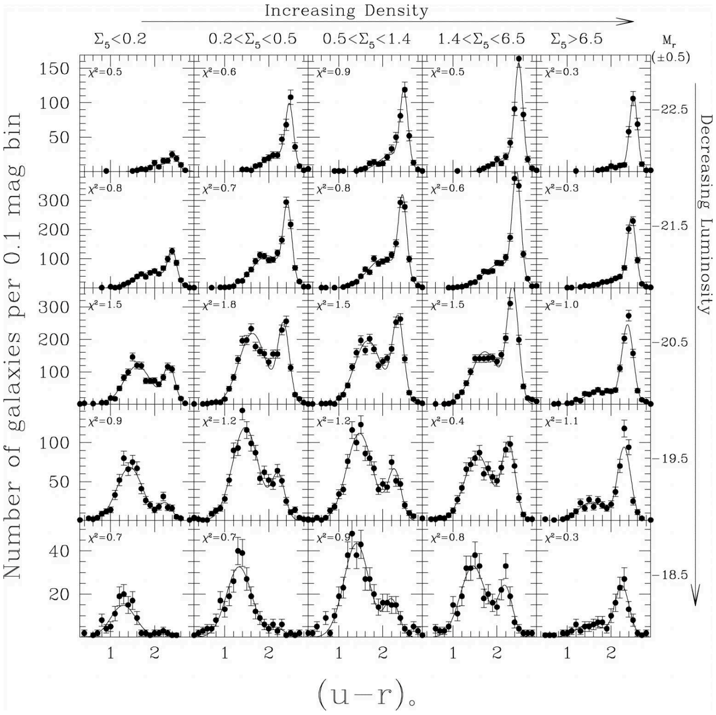

Fig. 16. Filled circles in each panel show the galaxy color distribution for the indicated 1 mag range of luminosity (right axis) and the range of local projected density, in units of Mpc^{-2}, shown on the top axis. The solid line is a double-Gaussian model, with the dispersion of each distribution a function of luminosity only. The reduced χ^2 of the fit is shown in each panel (from Balogh et al. 2004).

tremely low fraction of massive blue galaxies. To completely suppress the fraction of blue galaxies at the massive end of the distribution the AGN feedback (sect. 3.8) has been implemented in the SAMs, as shown in Fig. 15. This removes the residual fraction of gas left over at low redshift in the star formation histories of massive galaxies, completely quenching subsequent star formation (see the lower highlighted star formation history in Fig. 14) leaving the color distribution of massive galaxies ($M_r \leq -22$) completely dominated by the red branch.

In sum, the suppression of low-z star formation in massive halos originate from different effects:

- Their progenitors form in biased regions of the density field, have accelerated SFR at high redshift, convert their gas into stars at high redshift, leaving a small amount of gas available for SFR at low redshifts.
- Their progenitors undergo a larger number of major merging events, converting large fraction of gas into stars at $z \gtrsim 2$.
- The Cooling Function is smaller in large halos.
- AGN feedback quenches star formation from residual gas.

5.4. The environmental dependence

The properties of galaxies depend strongly on the environment where they reside. In Fig. 16 we show the color distribution as a function of the magnitude and of the environmental densities. While the mean colours and spread of the red and blue populations depends only weakly on environment, their relative abundance is a

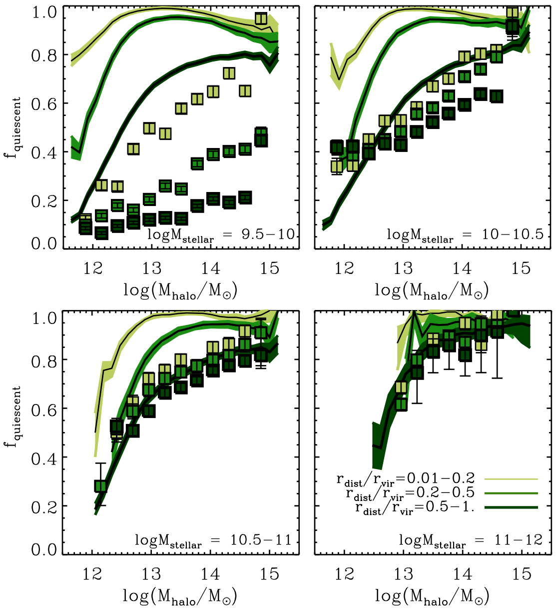

Fig. 17. Quiescent fractions of satellite galaxies are plotted versus the parent halo mass for observations (symbols) and the Guo (2011) SAM (lines with shaded areas). Different panels correspond to different stellar mass bins (from Hirschmann et al. 2014).

function of environment. In particular, while for bright galaxies the red fraction changes little with the environment, for low-luminosity galaxies it increases appreciably in the densest environments.

Such an environmental dependence is due to i) the biased galaxy formation effect discussed above (with the galaxies ending up in dense environments forming within biased regions of the density field); ii) to the larger number of merging events affecting galaxies in dense regions (converting rapidly the gas into stars at high redshifts thus leaving red objects at low z); iii) to the strangulation effect, i.e., the stripping of the gas from satellite galaxies when they are included in the host halo (sect. 3.6). Although models qualitatively reproduce the observed trends, their quantitative predictions concerning a) the width of the red sequence in clusters and b) the fraction of red satellite galaxies constitutes critical issues.

As for the former, the red sequence observed in galaxy clusters already at $z \approx 1$, is extremely tight (observed spread in color $\Delta_{U-V} \approx 0.2$, see Mei et al. 2009). Although recent models predict a tighter red sequence in dense environments the predicted width in galaxy clusters at $z \approx 1$ (corresponding to the most biased regions of the density field) is still ~ 5 times larger than the observed (Menci et al. 2008).

As for the fraction of red small-mass satellites, SAMs typically predict most (in fact, more than 80%, see Kimm et al. 2009) of satellite galaxies to be quiescent, with low specific star formation rates SSFR $\equiv \dot{m}_*/m_* \leq 10^{-11}$ yr^{-1}, while observations indicate a much lower fraction $\sim 30\%$ (see, e.g., Wetzel et al. 2013) for satellite galaxies with stellar mass in the range $10^8\,M_\odot \leq M_* \leq 10^{10}\,M_\odot$ within massive host halos ($M_{host} \simeq 10^{12.} - 10^{14}\,M_\odot$), as shown in Fig. 17. The discrepancy is generally ascribed to the implementation of the various baryonic processes contributing to the quenching of star formation in satellites, like the stripping of hot gas (strangulation, Larson et al.

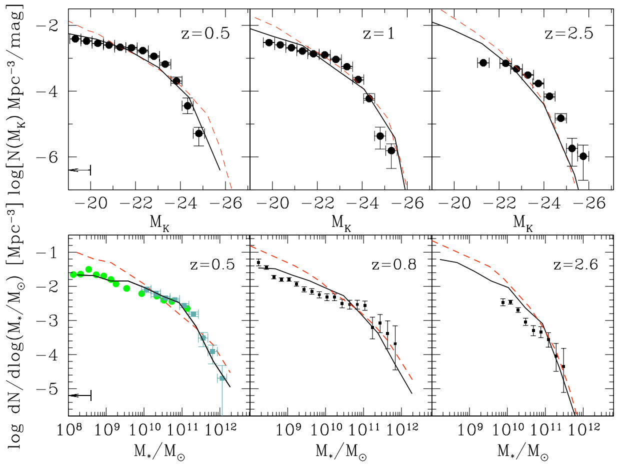

Fig. 18. Top Panel. The evolution of the K-band luminosity functions in the WDM cosmology (solid line) is compared with data from Cirasuolo et al. (2010). Dashed line refer to the standard CDM case. Bottom Panel: The evolution of the stellar mass function in the WDM cosmology (solid line) is compared with the standard CDM case (dashed); data in the leftmost panel are from Drory et al. (2004, squares) and Fontana et al. (2006, circles); data in all remaining panels are from Santini et al. (2012). In both the upper and the lower left panels, the arrows show the range of magnitudes and stellar masses corresponding to the free streaming mass.

1980; Cole et al. 2000; Balogh et al. 2000; Kawata & Mulchaey 2008; McCarthy et al. 2008) due to the pressure of the gas in the host halo. However, the persistence of such a problem in the most recent semi-analytic models (Hirschmann et al. 2012; Bower et al. 2012; Weinmann et al. 2012) and N-body hydrodynamical simulations (Weinmann et al. 2012; Hirschmann et al. 2014) indicates that it constitutes a major challenge for all CDM galaxy formation models, and constitutes a fundamental problem in understanding the evolution of low-mass galaxies (Weinmann et al. 2012).

6. Some open problems and perspectives

Despite the recent progress summarized in sect. 5.1-5.4, several problems still affect cosmological galaxy formation models. In particular, all models over-predict the number densities of low to intermediate stellar mass galaxies (especially at $z \gtrsim 1$, see sect. 5.2) and the fraction of passive satellite galaxies (see sect. 5.3). The most shared view is that such problems are related to the current implementation of the stellar feedback and of the environmental quenching processes. Although more refined treatments of feedback, gas stripping, of the ram pressure effects are surely required, providing firm solutions based on such developments still constitutes a challenging task.

As for the over-prediction on low-luminosity galaxies, reducing the number of detectable galaxies through feedback processes (see, e.g. Governato et al. 2012; Di Cintio et al. 2014, for feedback studies based on simulations) results in hosts too massive to be accommodated within measured galactic rotation curves (Papastergis et al. 2015), and still does not avoid the over-production of low-mass galaxies at redshifts $z \gtrsim 1$ (shown in sect. 5.2). As for the red fraction of satellites, a solution has been recently sought in the implementation of star formation (see, e.g., Wang et al. 2012), in reincorporation timescales of the hot gas ejected by SNae winds (Henriques et al. 2013), or in a delayed and gradual stripping of hot gas from satellites (Simha et al. 2009; Guo et al. 2011; Font et al.

2008), but none of the proposals proved to be completely successful. Indeed, the problem originates from the fact that the observed low red fraction of satellites implies long quenching times for the latter (see Wetzel et al. 2013), while all environmental processes considered so far are characterized by much shorter time scales. In particular, the gas stripping in satellite galaxies (calibrated through N-body simulations) seems to be inappropriate in providing the requited slow quenching times. The above discussion shows that the simultaneous matching of abundance and star formation properties of satellite galaxies is a major challenge of all CDM models. Thus, a growing attention is focusing on alternative models, which are characterized by a power spectrum with less power on small scales. In this context, assuming a Warm DM model (WDM, characterized by particles with mass $m_X \sim 1$ keV) could provide a simultaneous solution of the above problems. In fact, in this case the power spectrum is characterized by a steep cutoff at the dwarf galaxy scales (Bode et al. 2001), due to the free-streaming of the lighter DM particles. The corresponding lack of small-scale power results in a reduced dwarf galaxy abundance and shallower inner density profiles, which are in better agreement with observations (Macciò et al. 2012; Schneider et al. 2012; Lovell et al. 2012, 2014; Polisensky & Ricotti 2011; de Vega et al. 2014; Papastergis et al. 2015), while being indistinguishable from CDM on larger scales. In addition, the delayed collapse of small scale perturbations results into prolonged star formation histories of small-mass satellite galaxies providing a better match to the observed low fraction of red satellite galaxies. Several works have started to explore galaxy formation in a WDM Cosmology (see, e.g., Kang et al. 2013), showing that assuming a WDM spectrum corresponding to particles with mass $m_X \approx 1 - 3$ keV can provide a viable solution to the above mentioned problems concerning galaxy formation (see Fig. 18). Whether such a range for WDM masses is compatible with other cosmological and astrophysical constraints still constitutes a debated issue (see Viel et al. 2013; Garzilli et al. 2015; Abazajian et al. 2011; Watson et al. 2012, and references therein).

Acknowledgements. I acknowledge the organizers of the School of Astrophysics "F. Lucchin" 2014 for the perfect organization, the welcoming atmosphere, and the stimulating school program.

References

Abazajian, K. N., Calabrese, E., Cooray, A., et al. 2011, Astroparticle Physics, 35, 177
Baldry, I. K., Glazebrook, K., Brinkmann, J., et al. 2004, ApJ, 600, 681
Balogh, M. L., Baldry, I. K., Nichol, R., et al. 2004, ApJ, 615, L101
Balogh, M. L., Navarro, J. F., & Morris, S. L. 2000, ApJ, 540, 113
Benson, A. J., Bower, R. G., Frenk, C. S., et al. 2003, ApJ, 599, 38
Benson, A. J., et al. 2002, MNRAS, 333, 177
Binney, J. & Tremaine, S. 1987, Galactic dynamics
Blanton, M. R., et al. 2005, ApJ, 629, 143
Bode, P., Ostriker, J. P., & Turok, N. 2001, ApJ, 556, 93
Bouwens, R. J., Illingworth, G. D., Oesch, P. A., et al. 2011, ApJ, 737, 90
Bower, R. G., Benson, A. J., & Crain, R. A. 2012, MNRAS, 422, 2816
Bruzual, G. & Charlot, S. 2003, MNRAS, 344, 1000
Cavaliere, A. & Vittorini, V. 2000, ApJ, 543, 599
Chartas, G., et al. 2002, ApJ, 579, 169
Cirasuolo, M., McLure, R. J., Dunlop, J. S., et al. 2010, MNRAS, 401, 1166
Cole, S., et al. 2000, MNRAS, 319, 168
Cole, S., Norberg, P., Baugh, C. M., et al. 2001, MNRAS, 326, 255
Conselice, C. J. 2014, ARA&A, 52, 291
Cox, T. J., et al. 2008, MNRAS, 384, 386
Crenshaw, D. M., Kraemer, S. B., & George, I. M. 2003, ARA&A, 41, 117
Croton, D. J., Springel, V., White, S. D. M., et al. 2006, MNRAS, 365, 11
Daddi, E., Elbaz, D., Walter, F., et al. 2010, ApJ, 714, L118
De Lucia, G. & Blaizot, J. 2007, MNRAS, 375, 2

de Vega, H. J., Salucci, P., & Sanchez, N. G. 2014, MNRAS, 442, 2717
Dekel, A. & Silk, J. 1986, ApJ, 303, 39
Di Cintio, A., Brook, C. B., Dutton, A. A., et al. 2014, MNRAS, 441, 2986
Drory, N., Bender, R., Feulner, G., et al. 2004, ApJ, 608, 742
Eke, V. R., Cole, S., Frenk, C. S., & Patrick Henry, J. 1998, MNRAS, 298, 1145
Fabian, A. C. 2012, ARA&A, 50, 455
Font, A. S., Bower, R. G., McCarthy, I. G., et al. 2008, MNRAS, 389, 1619
Fontana, A., Salimbeni, S., Grazian, A., et al. 2006, A&A, 459, 745
Garzilli, A., Boyarsky, A., & Ruchayskiy, O. 2015, ArXiv
Genzel, R., Tacconi, L. J., Gracia-Carpio, J., et al. 2010, MNRAS, 407, 2091
Governato, F., Zolotov, A., Pontzen, A., et al. 2012, MNRAS, 422, 1231
Granato, G. L., Lacey, C. G., Silva, L., et al. 2000, ApJ, 542, 710
Gruppioni, C., Calura, F., Pozzi, F., et al. 2015, MNRAS, 451, 3419
Guo, Q., White, S., Boylan-Kolchin, M., et al. 2011, MNRAS, 413, 101
Henriques, B. M. B. & Thomas, P. A. 2010, MNRAS, 403, 768
Henriques, B. M. B., White, S. D. M., Thomas, P. A., et al. 2015, MNRAS, 451, 2663
Henriques, B. M. B., White, S. D. M., Thomas, P. A., et al. 2013, MNRAS, 431, 3373
Hirschmann, M., De Lucia, G., Wilman, D., et al. 2014, MNRAS, 444, 2938
Hirschmann, M., et al. 2012, MNRAS, 426, 237
Huang, J.-S., et al. 2003, ApJ, 584, 203
Kang, X., Macciò, A. V., & Dutton, A. A. 2013, ApJ, 767, 22
Kawata, D. & Mulchaey, J. S. 2008, ApJ, 672, L103
Kennicutt, Jr., R. C. 1998, ApJ, 498, 541
Kimm, T., Somerville, R. S., Yi, S. K., et al. 2009, MNRAS, 394, 1131
King, I. 1962, AJ, 67, 471
Klypin, A., Kravtsov, A. V., Valenzuela, O., & Prada, F. 1999, ApJ, 522, 82
Kochanek, C. S., Pahre, M. A., Falco, E. E., et al. 2001, ApJ, 560, 566
Kormendy, J. & Ho, L. C. 2013, ARA&A, 51, 511
Lacey, C. & Cole, S. 1993, MNRAS, 262, 627
Larson, R. B., Tinsley, B. M., & Caldwell, C. N. 1980, ApJ, 237, 692
Li, C. & White, S. D. M. 2009, MNRAS, 398, 2177
Lovell, M. R., Eke, V., Frenk, C. S., et al. 2012, MNRAS, 420, 2318
Lovell, M. R., Frenk, C. S., Eke, V. R., et al. 2014, MNRAS, 439, 300
Macciò, A. V., et al. 2012, MNRAS, 424, 1105
Madau, P. & Dickinson, M. 2014, ARA&A, 52, 415
Marchesini, D., van Dokkum, P. G., Förster Schreiber, N. M., et al. 2009, ApJ, 701, 1765
McCarthy, I. G., Frenk, C. S., Font, A. S., et al. 2008, MNRAS, 383, 593
Mei, S., Holden, B. P., Blakeslee, J. P., et al. 2009, ApJ, 690, 42
Menci, N., et al. 2002, ApJ, 575, 18
Menci, N., et al. 2008, ApJ, 686, 219
Menci, N., et al. 2006, ApJ, 647, 753
Menci, N., et al. 2014, A&A, 569, A37
Merloni, A. & Heinz, S. 2013, Evolution of Active Galactic Nuclei, ed. T. D. Oswalt & W. C. Keel, 503
Mo, H. J., Mao, S., & White, S. D. M. 1998, MNRAS, 295, 319
Monaco, P., Fontanot, F., & Taffoni, G. 2007, MNRAS, 375, 1189
Moore, B., et al. 1999, MNRAS, 310, 1147
Moster, B. P., Naab, T., & White, S. D. M. 2013, MNRAS, 428, 3121
Nagamine, K., et al. 2005a, ApJ, 627, 608
Nagamine, K., et al. 2005b, ApJ, 618, 23
Navarro, J. F., Frenk, C. S., & White, S. D. M. 1997, ApJ, 490, 493
Papastergis, E., et al. 2015, A&A, 574, A113
Peebles, P. J. E. 1993, Principles of Physical Cosmology
Pérez-González, P. G., Rieke, G. H., Villar, V., et al. 2008, ApJ, 675, 234
Planck Collaboration, Ade, P. A. R., Aghanim, N., et al. 2014, A&A, 571, A16
Polisensky, E. & Ricotti, M. 2011, Phys. Rev. D, 83, 043506
Press, W. H. & Schechter, P. 1974, ApJ, 187, 425
Richstone, D., Ajhar, E. A., Bender, R., et al. 1998, Nature, 395, A14

Sanders, D. B. & Mirabel, I. F. 1996, ARA&A, 34, 749

Santini, P., Fontana, A., Grazian, A., et al. 2012, A&A, 538, A33

Santini, P., Maiolino, R., Magnelli, B., et al. 2014, A&A, 562, A30

Saslaw, W. C. 1985, Gravitational physics of stellar and galactic systems

Schmidt, M. 1959, ApJ, 129, 243

Schneider, A., et al. 2012, MNRAS, 424, 684

Shankar, F., Weinberg, D. H., & Miralda-Escudé, J. 2009, ApJ, 690, 20

Simha, V., Weinberg, D. H., Davé, R., et al. 2009, MNRAS, 399, 650

Somerville, R. S. & Davé, R. 2015, ARA&A, 53, 51

Somerville, R. S. & Kolatt, T. S. 1999, MNRAS, 305, 1

Somerville, R. S. & Primack, J. R. 1999, MNRAS, 310, 1087

Sutherland, R. S. & Dopita, M. A. 1993, ApJS, 88, 253

Tegmark, M. & Zaldarriaga, M. 2002, Phys. Rev. D, 66, 103508

Tormen, G. 1997, MNRAS, 290, 411

Viel, M., et al. 2013, Phys. Rev. D, 88, 043502

Wang, L., Weinmann, S. M., & Neistein, E. 2012, MNRAS, 421, 3450

Warren, M. S., et al. 1992, ApJ, 399, 405

Watson, C. R., Li, Z., & Polley, N. K. 2012, Journal of Cosmology and Astroparticle Physics, 3, 018

Weinmann, S. M., Pasquali, A., Oppenheimer, B. D., et al. 2012, MNRAS, 426, 2797

Wetzel, A. R., et al. 2013, MNRAS, 432, 336

White, S. D. M. & Frenk, C. S. 1991, ApJ, 379, 52

White, S. D. M. & Rees, M. J. 1978, MNRAS, 183, 341

Yu, Q. & Tremaine, S. 2002, MNRAS, 335, 965